

A phenomenological model for the solidification of eutectic and hypoeutectic alloys including recalescence and undercooling

M. Chiumenti, M. Cervera, E. Salsi and A. Zonato
International Center for Numerical Methods in Engineering (CIMNE)
Universitat Politècnica de Catalunya (UPC), Barcelona, Spain
michele@cimne.upc.edu

KEYWORDS: Thermal analysis, solidification model, eutectic and hypoeutectic cast-iron alloys, recalescence, undercooling.

Abstract

In this work a novel phenomenological model is proposed to study the liquid-to-solid phase change of eutectic and hypoeutectic alloy compositions.

The objective is to enhance the prediction capabilities of the solidification models based on a-priori definition of the solid fraction as a function of the temperature field. However, the use of models defined at the metallurgical level is avoided to minimize the number of material parameters required. This is of great industrial interest because, on the one hand, the classical models are not able to predict recalescence and undercooling phenomena, and, on the other hand, the complexity as well as the experimental campaign necessary to feed most of the microstructure models available in the literature make their calibration difficult and very dependent on the chemical composition and the treatment of the melt.

Contrarily, the proposed model allows for an easy calibration by means of few parameters. These parameters can be easily extracted from the temperature curves recorded at the hot spot of the Quick-Cup test, typically used in the Differential Thermal Analysis (DTA) for the quality control of the melt just before pouring.

The accuracy of the numerical results is assessed by matching the temperature curves obtained via DTA of eutectic and hypoeutectic alloys. Moreover, the model is validated in more complex casting experiments where the temperature is measured at different thermocouple locations and the metallurgical features such as grain size and nucleation density are obtained from an exhaustive micrography campaign.

The remarkable agreement with the experimental evidence validates the predicting capabilities of the proposed model.

1 Introduction

One of the challenges of today's casting practice is the quality control of the manufacturing process and the final properties of the casting products. The mechanical properties of cast iron strongly depend on the solidification microstructure as well as the porosity induced by the shrinkage phenomena. The chemical composition of the alloy, the inoculation treatment of the melt and the overall cooling conditions are the main process parameters that influence the solidification process. Complex casting geometries are characterized by a wide range of cooling rates due to the thickness distribution of the casting components and complex heat loss mechanisms, leading to wide differences in the final metallurgical properties at different points of the casting part. Therefore, an accurate study of solidification and cooling conditions is essential for the improvement of the casting process and the metallurgical quality of the parts.

In order to study these phenomena, the numerical simulation of the thermal process is a consolidated industrial practice thanks to the use of dedicated software allowing for the heat transfer analysis of foundry components. The latent heat released during the solidification is the key point of the phase change transformation. On the one hand, the total amount of latent heat is assumed as a material property. On the other hand, the heat release mechanism is controlled by the evolution of the solid fraction during the solidification process.

In the first attempts of predicting the solidification phenomena, the solid fraction has been assumed as an explicit function of the alloy temperature. Several methods have been proposed such as the effective specific heat method [36], [21], [40], the enthalpy method [24], [29], [45] or the temperature recovery method [42], among others. These methods assume an explicit relationship between the temperature at each point of the melt and the amount of latent heat released. The solid fraction function can be obtained by Differential Thermal Analysis (DTA) measurements [19], [38], using the Back Diffusion (BD) model [9], or adopting analytical laws such as the Lever rule or Scheil rules [44]. All these methods take into account the *effects* induced by the actual chemical composition of the alloy but, generally, ignore the influence of the local cooling rates as well as any kinetic phenomena during the solidification. Consequently, undercooling and recalescence phenomena are typically impossible to be predicted and pose serious numerical inconveniences when dealing with eutectic compositions (e.g. isothermal phase-changes).

The numerical simulation of casting processes experienced a significant step forward by introducing models based on the prediction of the microstructure evolution. As a first approximation, the *mesoscale* models express the fraction of solid during the solidification by estimating an *average* nucleation density and the corresponding grain growth for each phase. Typically, both the nucleation density and grain growth are related to kinetic parameters such as the cooling rates of the melt, the undercooling effects and the specific melt treatment such as the inoculation strategy. Starting from the original works of Oldfield [37] on the nucleation law for cast-iron, to the models proposed by Stefanescu ([46], [47], [49]), Rappaz ([40], [51]), Lacaze ([32], [33], [34]), Svensson [52], Celentano

([39], [11], [12], [13], [14], [25]), Dardati ([27], [28], [10], [53]), the complexity of the subjacent microstructure has been incremented progressively.

More sophisticated models, such as the cellular automata technique ([30], [31], [18] and [35]), describe the solidification phenomena at the *microscale* level, combining both deterministic and probabilistic laws in order to study the evolution of each single grain and the grain-to-grain interaction within a more realistic description of the microstructure. Using these microstructure models, it is possible to achieve a realistic visualization of the dendritic phase growing during the solidification, the interaction with the eutectic nuclei and the influence of the carbon content and its diffusion.

Both mesoscale and microscale approaches have some drawbacks. On the one hand, mesoscale models are very much dependent on the actual chemical composition of the alloy and the technological treatment of the melt, requiring a tedious calibration process of the sophisticated evolution laws proposed in the last years. Furthermore, they still rely on coarse approximation of the grain shape (typically equiaxial grains) and grain interactions, as well as on empirical nucleation laws. On the other hand, microscale models can produce very accurate predictions but the upscaling process to the macroscale, where the heat transfer analysis is modelled, and the necessary computational resources, make their use unaffordable when facing the study of complex industrial components.

In this paper a different approach to the solidification problem is proposed. The main idea consists of assuming a *macroscale* model, where the solidification depends on the definition of an *ad-hoc evolution law for the solid fraction*. Hence, the latent heat release is not written as an explicit function of the local temperature field, but it relies on the time integration of an evolution law for the solid fraction. This evolution law takes into account the chemical composition (i.e. the equivalent carbon content) as well as the cooling rate at each point of the casting. Therefore, the main idea is to characterize the solidification process to obtain the most realistic temperature evolution without introducing any explicit relationship with the subjacent microstructure. The phase change model is kept as simple as possible, regardless of the complexity of the phenomena taking place at the microscale while *capturing their effects* at the macroscale. The alloy composition as well as the melt treatment are accounted by experimental calibration (e.g. matching the numerical result of the model with the temperature evolution recorded by a thermocouple at the hot-spot in a *Quick-Cup* test, typically used in DTA).

The same idea has been successfully used to study the thermochemical hydration process of concrete ([23], [15]). The parallelism with the metal casting process is evident: the hydration of concrete is a highly exothermic and thermally activated reaction where the diffusion of water and the formation of hydrates are the dominant mechanisms at the microscale level defining the reaction kinetics. Also in this case, the main objective is to capture the *phenomenological* aspects of the process without explicitly referring to the physical-chemical phenomena occurring at the microscale level.

In the next Section, a review of the equations used for the heat transfer analysis is presented. The solidification model for the eutectic and the hypoeutectic

phase-changes is introduced in Sections 3 and 4, respectively. The models are enhanced by coupling the solidification with the characterization of the thermo-physical material properties used in the heat transfer analysis. This is achieved by introducing a mixture rule based on the growth of the different phases in the melt. Finally, Section 5 shows the calibration and validation work carried out. In the casting benchmarks proposed both the chemical composition of the melt and the thermal module of the components are modified to demonstrate the prediction accuracy of the proposed model.

2 Heat transfer analysis

Both the solidification and the cooling phases are controlled by the *balance of energy equation* ([26]). This governing equation can be stated as:

$$\frac{dH}{dT} = -\nabla \cdot \mathbf{q} \quad (1)$$

where $\frac{dH}{dT}$ is the enthalpy rate (per unit of volume) and \mathbf{q} is the heat flux.

The enthalpy $H(T, f_L)$ is the state variable defined as a function of the temperature, T , and the liquid fraction, f_L . Hence, the enthalpy rate in (1) can be written as:

$$\frac{dH}{dT}(T, f_L) = \frac{\partial H}{\partial T} \dot{T} + \frac{\partial H}{\partial f_L} \dot{f}_L = C \frac{dT}{dt} + L \frac{df_L}{dt} \quad (2)$$

where $C = \frac{\partial H}{\partial T}$ is the heat capacity and $L = \frac{\partial H}{\partial f_L}$ is the latent heat released during the phase-change process.

The heat capacity of the material is defined as: $C = \rho c$, the product of the material density, ρ , and the specific heat, c .

The heat flux (per unit of surface) \mathbf{q} , is computed as a function of the temperature gradient through the Fourier's law as:

$$\mathbf{q} = -k \nabla T \quad (3)$$

where k is the thermal conductivity.

The solution of the thermal problem consists of enforcing the weak form of the balance of energy equation. This means integrating Eq. (1) over the open and bounded volume V , closed by the smooth boundaries $S = S_T \cup S_q$ where the corresponding boundary conditions are defined in terms of either prescribed temperature ($T = \bar{T}$) on S_T or prescribed heat flux ($-k \nabla T \cdot \mathbf{n} = \bar{q}$) through the surface S_q with external normal \mathbf{n} . Suitable initial conditions for the transient thermal problem are defined in terms of initial temperature field: $T(t=0) = T_0$.

The resulting weak (integral) form of the energy balance equation used for the heat transfer analysis, can be written as ([16], [1], [2], and [3]):

$$\int_V \left[\left(C \frac{dT}{dt} + L \frac{df_L}{dt} \right) \delta T \right] dV + \int_V [k \nabla T \cdot \nabla (\delta T)] dV = W_{ther}^{ext} \quad \forall \delta T \quad (4)$$

where δT are the variations of the temperature field (test functions) compatible with the Dirichlet's boundary conditions and W^{ext} denotes the external work of the thermal loads:

$$W^{ext}(T) = - \int_{S_q} [(\bar{q} + q_{cond} + q_{conv} + q_{rad}) \delta T] dS \quad (5)$$

In Eq. (5), \bar{q} represents the prescribed heat flux (Neumann's condition) while q_{conv} and q_{rad} are the heat fluxes by convection and by radiation, responsible of the heat loss through the body surfaces in contact with the environment. The effects of the heat convection can be taken into account using Newton's law (Robin's condition) in the form [20]:

$$q_{cond} = h_{conv}(T - T_{env}) \quad (6)$$

where $h_{conv}(T)$ is the (temperature dependent) Heat Transfer Coefficient (HTC) by convection and T_{env} is the ambient temperature.

The radiation heat flux can be computed using Stefan–Boltzmann's law as a function of the casting surface temperature, T , and the ambient temperature as:

$$q_{rad} = \sigma_{rad} \varepsilon_{rad} (T^4 - T_{env}^4) \quad (7)$$

where σ_{rad} is the Stefan–Boltzmann constant and ε_{rad} is the emissivity parameter.

Finally, the heat flux due to the heat conduction process between the casting and the mould surfaces, q_{cond} , can be taken into account using Newton's law as:

$$q_{cond} = h_{cond}(T - T_{mould}) \quad (8)$$

where h_{cond} is the HTC by conduction between the casting and the mould surfaces in contact, and T_{mould} is the mould temperature.

Remark 1 *The HTC by conduction is defined as the inverse of the corresponding thermal resistivity and it depends on different parameters at the contact interface such as the contact pressure and the surfaces roughness, among others. When the contact is between metallic materials (e.g. solidification of aluminum casting in permanent steel moulds), the HTC assumes very high values around 2000 – 3000 [W/m²K]. When using a sand mould, this value can be reduced to 100 – 500 [W/m²K] (see [11], [15], [20]).*

Remark 2 *Stefan–Boltzmann's law can be rewritten as:*

$$q_{rad} = h_{rad}(T - T_{env}) \quad (9)$$

where $h_{rad}(T)$ is the (temperature dependent) HTC by radiation defined as:

$$h_{rad}(T) = \sigma_{rad} \varepsilon_{rad} (T^3 + T^2 T_{env} - T T_{env}^2 - T_{env}^3) \quad (10)$$

This format is interesting for two reasons: firstly, because it is possible to linearize the contribution of the heat radiation term as:

$$q_{rad} = h_{rad}(T^n)(T^{n+1} - T_{env}) \quad (11)$$

where $T^{n+1} = T(t^{n+1})$ is the current temperature at time t^{n+1} , and $T^n = T(t^n)$ is temperature in the previous time-step. The second reason is that it is extremely difficult to separate the heat losses due to the convection and the radiation mechanisms. Hence, the numerical model may use a unique HTC accounting for both heat convection and radiation terms, as:

$$q_{loss} = h_{loss}(T - T_{env}) \quad (12)$$

where $h_{loss}(T)$ is the (temperature dependent) HTC accounting for the total heat loss through the surrounding environment.

Remark 3 The thermal problem in Eq.(4) can be solved using different numerical methods such as: Finite Volume (FV), Finite Differences (FD) or Finite Element (FE) methods, among others. In this work, the results obtained in both the numerical caibration and the following validation strategy refer to a spatial FE discretization and a Backward-Euler time integration of the thermal problem. Hence, after meshing the integration domain, V , is split into (ne) elements as: $V = \sum_{e=1}^{ne} V_{(e)}$. The temperature field within each element is obtained from the nodal values $\mathbf{T}_{(e)}$ through the interoplation (shape) functions $\mathbf{N}_{(e)}$, as: $T_{(e)} = \mathbf{N}_{(e)} \mathbf{T}_{(e)}$. Moreover, following the Galerkin method, the test (weight) function are chosen as: $\delta T_{(e)} = \mathbf{N}_{(e)}$. Hence, the dicrete form of the balance of energy equation can be written as:

$$\begin{aligned} \sum_{e=1}^{ne} \int_{V_{(e)}} \mathbf{N}_{(e)}^T \left[C \left(\frac{T_{(e)}^{(n)} - T_{(e)}^{(n-1)}}{\Delta t} \right) + L \left(\frac{f_L^{(n)} - f_L^{(n-1)}}{\Delta t} \right) \right] dV_{(e)} + \\ \sum_{e=1}^{ne} \int_{V_{(e)}} k \mathbf{B}_{(e)}^T \nabla T_{(e)} dV_{(e)} = \sum_{e=1}^{ne} W_{(e)}^{ext} \end{aligned} \quad (13)$$

where the $\mathbf{B}_{(e)} = \nabla \mathbf{N}_{(e)}$ and $\sum_{e=1}^{ne}$ stands for the assembling procedure.

3 Eutectic model

The reference material in this work is SG cast-iron also known as ductile iron or nodular iron. This material plays a key role for many engineering applications in automotive and aerospace industry due to the good combination of high strength, good creep and fatigue resistance. Focusing on the SG eutectic composition, the uni-nodular theory for stable equiaxial solidification assumes that after the nucleation the graphite nodules are encapsulated by the austenite

dendrites and a constant ratio between the size of the austenite shell and the graphite nodule is maintained during the grain growth ([26], [46], [13], [8]).

During the phase transformation, the volume of the casting, V , can be split into liquid and solid phases as: $V = V_L + V_S$. The liquid and solid fractions are defined as: $f_L = \frac{V_L}{V}$ and $f_S = \frac{V_S}{V}$, respectively, so that: $f_L + f_S = 1$. The evolution of the liquid fraction $\frac{df_L}{dt}$ or, alternatively, the solid fraction rate: $\frac{df_S}{dt} = -\frac{df_L}{dt}$, defines the phase-change, that is, how the latent heat is absorbed or released during the transformation. The phase transformation is monitored at each point of the domain, so that the solidification analysis depends on the *local* evolution of the temperature field.

Hereafter, this solid phase is referred to as the eutectic phase, f_E . Therefore, $f_S = f_E$, being $0 \leq f_E \leq 1$. Hence, the weak form of the balance of energy equation (4) is modified by associating the latent heat release with the grain growth of the eutectic phase: $L \frac{df_L}{dt} = -L \frac{df_E}{dt}$.

Figure 1 shows the temperature curve and its first derivative as recorded in a typical DTA for an eutectic alloy. In this figure, different key points are shown:

- T_L^{start} indicates the beginning of the solidification. For an eutectic composition T_L^{start} is also assumed as the beginning of the eutectic phase $T_L^{start} = T_E^{start}$. This value corresponds to a local minimum in the curve of the first derivative of the temperature;
- $\left. \frac{dT}{dt} \right|_{T=T_E}$ is the cooling rate used to characterize the nucleation law (see Eq. 19);
- T_E^{min} and T_E^{max} are the temperatures corresponding to the local minimum and maximum of the eutectic transformation. Hence, the first derivative of the temperature curve is null at these points;
- T_S indicates the solidus temperature and corresponds to a further local minimum in the curve of the first derivative of the temperature.

In this work, the transformation kinetics of the eutectic phase is defined by the following evolution law:

$$\frac{df_E}{dt} = A_E (1 - f_E) f_E \quad f_E(t=0) = f_E^0 \quad (14)$$

This is an Avrami-type equation [4],[5],[6] which results into the characteristic *s*-shaped or sigmoidal profile where the transformation rates are slow at the beginning and at the end of the transformation but rapid in between (see Figure 2). The initial slow rate can be attributed to the nucleation process and the first growing phase which can be observed at the microscale, once the melt cools down from the pouring temperature to the eutectic temperature. Note that, an initial value $f_E(t=0) = f_E^0$ has been defined to let the transformation start. This initial fraction can be associated to the size of the graphite nodules at the nucleation start (e.g. the size of the inoculant particle after the solubilization into the melt). During the intermediate period the transformation is much

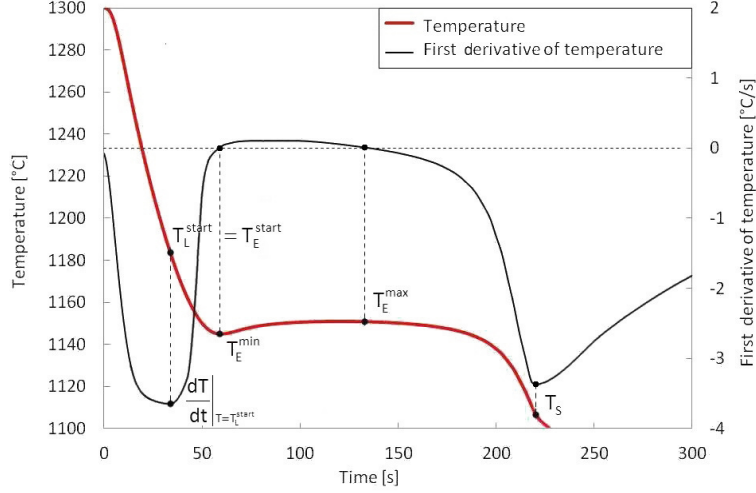


Figure 1: Temperature evolution and its first derivative obtained from the DTA of an Eutectic solidification process. Identification of the highlight temperatures used for the characterization of the Eutectic solidification model.

faster as the eutectic phase grows in the liquid without any mutual interaction. Later, the eutectic grains begin to get in contact among them slowing down the transformation. The maximum value of the transformation rate is controlled by the (temperature-dependent) function $A_E(T)$, defined as:

$$A_E(T) = \beta_E \left(\frac{\Delta T_E}{\Delta T_E^{crit}} \right)^{\gamma_E} \quad (15)$$

where $\Delta T_E = \langle T_E^{start} - T \rangle$ is referred to eutectic undercooling, being T_E^{start} the temperature threshold to initiate the eutectic transformation (see Figure 1), while β_E and γ_E are material parameters of the model. Expression (15) is normalized by introducing the critical undercooling parameter ΔT_E^{crit} . The Macaulay brackets, $\langle \cdot \rangle$, imply that $\Delta T_E = 0$ if $T > T_E^{start}$. The eutectic transformation begins when $T \leq T_E^{start}$ and the higher is the undercooling, the faster is the transformation.

The process is paused, $\frac{df_E}{dt} = 0$, in case of recalescence. Recalescence is a phenomenon that may occur when the latent heat released during the phase change is higher than the heat extraction during the cooling process, provoking a *local* increment of the temperature.

Remark 4 *As an alternative to equation (14), the following equivalent format*

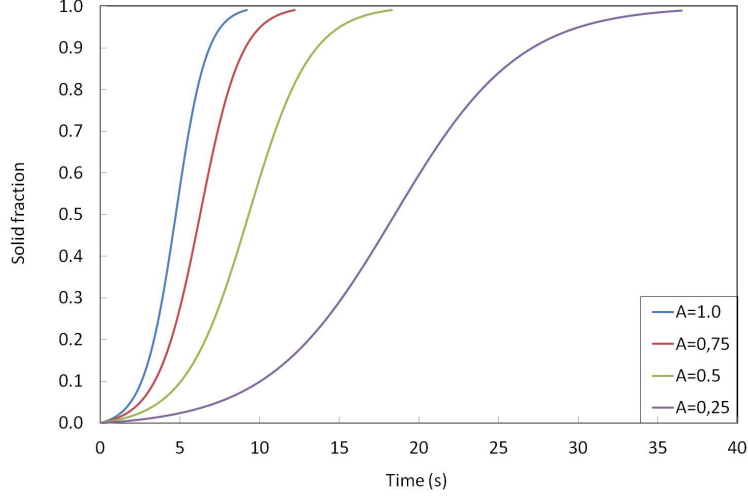


Figure 2: Solid fraction evolution as a function of the transformation rate parameter.

can be used:

$$\frac{df_E}{dt} = A_E (1 - f_E) (f_E^0 + f_E) \quad f_E(t=0) = 0 \quad (16)$$

where the natural initial condition: $f_E(t=0) = 0$ is recovered.

Remark 5 The proposed evolution law can be enhanced by adding an exponential term as shown in the following expression [15]:

$$\frac{df_E}{dt} = A_E (1 - f_E) (f_E^0 + f_E) \exp(-\delta_E f_E) \quad f_E(t=0) = 0 \quad (17)$$

being δ_E a new parameter of the model able to anticipate the peak corresponding to the maximum transformation rate (see Figure 3). Hence, the transformation is faster at the beginning of the phase-change while slowing down in the final part. This is a more realistic model in accordance to the experimental evidence.

Next, the average grain size, R_E , of the eutectic phase is computed from the current value of the eutectic fraction, f_E . Assuming an *equiaxial* shape for the grains, it is possible to write:

$$f_E = \frac{4\pi}{3} N_E R_E^3 \quad (18)$$

where N_E is the nucleation density. In this work an *instantaneous* nucleation law is assumed in the general form ([47],[49]):

$$N_E = k_1 + k_2 \left(\dot{T}_E \right)^m \quad (19)$$

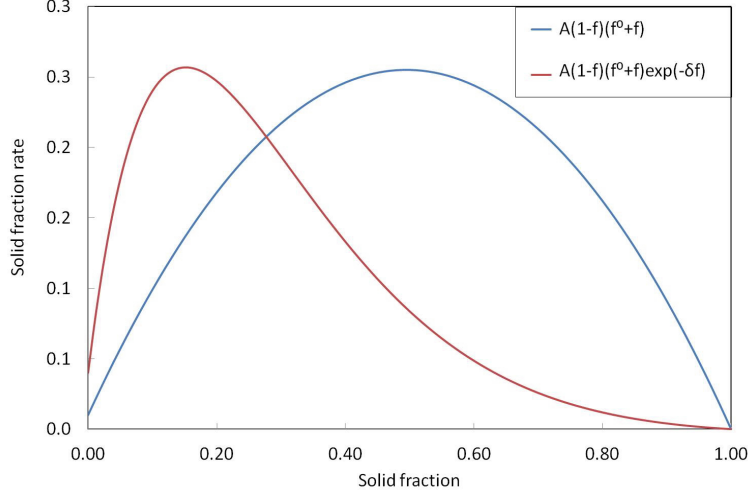


Figure 3: Solid fraction rate during the solidification process with or without considering the exponential term.

where $\dot{T}_E = \left. \frac{dT}{dt} \right|_{T=T_E}$ is the cooling rate of the liquid phase at the eutectic temperature (see Figure 1), while k_1 , k_2 and m are coefficients of the nucleation law depending on the composition of the melt and on the inoculation treatment.

This given, the average grain size of the eutectic phase is computed as [48]:

$$R_E = \sqrt[3]{\frac{3}{4\pi} \frac{f_E}{N_E}} \quad (20)$$

Remark 6 *The microstructure features, as the nucleation density and the grain size, are obtained a-posteriori contrariwise to the practice in the mesoscale approach.*

The model is complemented by defining a *mixture rule* accounting for the thermo-physical material properties of the different phases which coexist during the solidification process. According to the liquid and eutectic fractions, it is possible to compute the thermal conductivity and the heat capacity of the melt, k and C , respectively, as:

$$k = \sum_{i=1}^{nc} k_i f_i = k_L f_L + k_E f_E \quad (21)$$

$$C = \sum_{i=1}^{nc} C_i f_i = C_L f_L + C_E f_E \quad (22)$$

| Algorithm for the Eutectic model | |
|---|--|
| Initialize: | |
| $T_{(e)}^{(o)} = T_o$ | |
| $f_E^{(o)} = f_E^0$ | |
| Loop on time-steps: $n = 1, \text{number-of-time-steps}$ | |
| Compute the eutectic fraction: | |
| $A_E^{(n-1)} = \beta_E \left(\frac{\langle T_E^{start} - T_{(e)}^{(n-1)} \rangle}{\Delta T_E^{crit}} \right)^{\gamma_E}$ | |
| $f_E^{(n)} = f_E^{(n-1)} + A_E^{(n-1)} \left(1 - f_E^{(n-1)} \right) f_E^{(n-1)} \Delta t$ | |
| Update liquid & solid fractions: | |
| $f_S^{(n)} = f_E^{(n)}$ | |
| $f_L^{(n)} = 1 - f_S^{(n)}$ | |
| Update thermo-physical properties: | |
| $C^{(n)} = C_L f_L^{(n)} + C_E f_E^{(n)}$ | |
| $k^{(n)} = k_L f_L^{(n)} + k_E f_E^{(n)}$ | |
| Solve thermal problem: | |
| $\sum_{e=1}^{ne} \int_{V_{(e)}} \mathbf{N}_{(e)}^T \left[C^{(n)} \left(\frac{T_{(e)}^{(n)} - T_{(e)}^{(n-1)}}{\Delta t} \right) + L \left(\frac{f_L^{(n)} - f_L^{(n-1)}}{\Delta t} \right) \right] dV_{(e)} +$ $\sum_{e=1}^{ne} \int_{V_{(e)}} k^{(n)} \mathbf{B}_{(e)}^T \nabla T_{(e)}^{(n)} dV_{(e)} = \sum_{e=1}^{ne} W_{(e)}^{ext}$ | |
| Compute actual grain size: | |
| $N_E^{(n)} = k_1 + k_2 \left(\dot{T}_E^{(n)} \right)^m$ | |
| $R_E^{(n)} = \sqrt[3]{\frac{3}{4\pi} \frac{f_E^{(n)}}{N_E^{(n)}}}$ | |
| End loop | |

Table 1: Algorithm to solve the solidification analysis using the eutectic model

The step-by-step algorithm to solve the solidification problem for an eutectic alloy is presented in Table 1.

Remark 7 *The mixture rule establishes a direct relationship between the values of the thermophysical properties and the evolution of the phase transformation process. Typically, temperature-dependent tables are defined for each material property within the full temperature range, from the melting to the ambient temperature. Instead, the use of the mixture rule is sufficient to characterize the material behavior in terms of the evolution of the different phases evolving during the solidification and cooling processes.*

4 Hypo-Eutectic model

The proposed model can be extended to deal with hypo-eutectic alloys. In this case, two different transformations are taking place during the solidification process:

1. Firstly, the *dendritic phase*, referred to as the *primary austenite* (γ'), occurs. Its formation starts at the liquidus temperature, T_L^{start} , to finish at T_E^{start} , with the nucleation of the eutectic phase.
2. Later, the *eutectic phase* starts at T_E^{start} temperature, presents its maximum growth at the eutectic temperature, T_E , to terminate at the solidus temperature, T_S . The eutectic phase of the SG cast-iron is characterized by graphitic nuclei surrounded by the secondary austenite (γ'') while in the case of *Lamellar* cast iron (LG) there are graphite flakes surrounded by the secondary austenite [41].

Figure 4 shows temperatures T_L^{start} , T_E^{start} and T_S as recorded in the DTA of a hypoeutectic alloy, and corresponding to local minima in the curve of the first derivative of the temperature evolution during the phase transformation. In this figure, the eutectic plateau is characterized by T_E^{min} and T_E^{max} where the first derivative vanishes.

This given, the solid fraction is obtained adding the contributions of the dendritic phase f_D , and the eutectic phase f_E , as:

$$f_S = f_D + f_E \quad (23)$$

The partition ratio, θ , is introduced to establish the volumetric partition between these two phases, as:

$$0 \leq f_D \leq 1 - \theta \quad (24)$$

$$0 \leq f_E \leq \theta \quad (25)$$

This ratio is defined as a function of the chemical composition of the alloy. The model adopts the ratio between the actual *equivalent* carbon concentration, C_{eq} (including the effects of the *Si* segregation) and the carbon content, C_e , of the eutectic composition:

$$\theta = \left(\frac{C_{eq}}{C_e} \right)^\beta \quad \leftarrow \quad C_{eq} \leq C_e \quad (26)$$

where β is a parameter of the model.

Consequently, the solid fraction is computed as:

$$f_S = (1 - \theta) f_D^* + \theta f_E^* \quad (27)$$

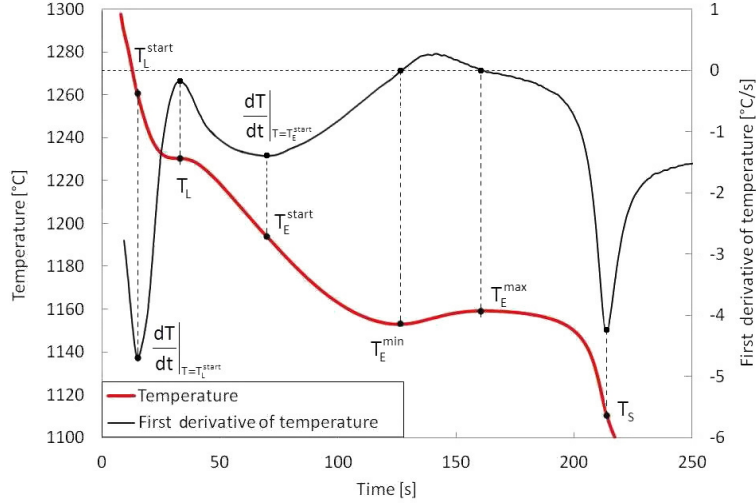


Figure 4: Temperature evolution and its first derivative obtained from the DTA of a hypoeutectic solidification process. Identification of the highlight temperatures used for the characterization of the hypoeutectic solidification model.

where $0 \leq f_D^* \leq 1$ and $0 \leq f_E^* \leq 1$ are the normalized dendritic and the eutectic fractions, respectively, that is:

$$f_D = (1 - \theta) f_D^* \quad (28)$$

$$f_E = \theta f_E^* \quad (29)$$

The latent heat release in the balance of energy equation (4) for a hypoeutectic alloy is computed taking into account the transformation kinetics of both phases as:

$$L \frac{df_L}{dt} = -L \left(\frac{df_D}{dt} + \frac{df_E}{dt} \right) = -L \left[(1 - \theta) \frac{df_D^*}{dt} + \theta \frac{df_E^*}{dt} \right] \quad (30)$$

The transformation kinetics of the dendritic and the eutectic phases are defined by the corresponding Avrami-type evolution laws:

$$\frac{df_D^*}{dt} = A_D (1 - f_D^*) (f_D^0 + f_D^*) \exp(-\delta_D f_D^*) \quad (31)$$

$$\frac{df_E^*}{dt} = A_E (1 - f_E^*) (f_E^0 + f_E^*) \exp(-\delta_E f_E^*) \quad (32)$$

where f_D^0 and f_E^0 are the initial dendritic and eutectic fractions at their respective nucleation time.

The transformation rates are controlled by the (temperature-dependent) functions A_D and A_E , respectively, and defined as:

$$A_D(T) = \beta_D \left(\frac{\Delta T_D}{\Delta T_D^{crit}} \right)^{\gamma_D} \quad (33)$$

$$A_E(T) = \beta_E \left(\frac{\Delta T_E}{\Delta T_E^{crit}} \right)^{\gamma_E} \quad (34)$$

On the one side, the dendritic growth depends on the value of undercooling, ΔT_D , defined as:

$$\Delta T_D = \langle \bar{T}_L - T \rangle \quad (35)$$

where \bar{T}_L is the actual liquidus temperature which is varying because of the carbon segregation. Its value is updated according to the solidification evolution using the following lever rule:

$$\bar{T}_L = (1 - f_S) T_L^{start} + f_S T_E^{start} \quad (36)$$

On the other side, the transformation rate of the eutectic phase depends on the undercooling with respect to the eutectic temperature:

$$\Delta T_E = \langle T_E^{start} - T \rangle \quad (37)$$

It is interesting to observe that the Eutectic Model is a particular case of the Hypoeutectic Model. If for the actual alloy $C_{eq} = C_e$ than the partition ratio: $\theta = 1$, and consequently: $f_S = f_E$. Hence, the solid fraction is computed according to the evolution of the eutectic phase, only. Note that when $T_L^{start} \rightarrow T_E^{start}$ then $\bar{T}_L \rightarrow T_E^{start}$ meaning that the dendritic phase is negligible and the the solidification is characterized by the nucleation of the eutectic phase and following grain growth.

Finally, the mixture rule used to compute the thermo-physical properties accounts for both eutectic and dendritic phases, as:

$$k = \sum_{i=1}^{nc} k_i f_i = k_L f_L + k_D f_D + k_E f_E \quad (38)$$

$$C = \sum_{i=1}^{nc} C_i f_i = C_L f_L + C_D f_D + C_E f_E \quad (39)$$

The corresponding step-by-step algorithm to solve the solidification problem of a hypo-eutectic alloy is shown in Table 2.

5 Validation strategy

In this Section, three different benchmarks are presented to validate the model proposed for the solidification process of cast iron alloys in sand molds. They are: The *Quick-Cup* test, the *Y-Shape* test and the *Cubes* test. These benchmarks

| Algorithm for the Hypo-eutectic model | |
|--|---|
| Initialize: | |
| | $T_{(e)}^{(o)} = T_o$ |
| | $f_D^{(o)} = f_D^0$ |
| | $f_E^{(o)} = f_E^0$ |
| Loop on time-steps: $n = 1, \text{number-of-time-steps}$ | |
| Compute the actual liquidus temperature: | |
| | $\bar{T}_L^{(n-1)} = (1 - f_S^{(n-1)}) T_L^{start} + f_S^{(n-1)} T_E^{start}$ |
| Update the dendritic & eutectic fractions: | |
| | $A_D^{(n-1)} = \beta_D \left(\frac{\langle \bar{T}_L^{(n-1)} - T_{(e)}^{(n-1)} \rangle}{\Delta T_D^{crit}} \right)^{\gamma_D}$ |
| | $A_E^{(n-1)} = \beta_E \left(\frac{\langle T_E^{start} - T_{(e)}^{(n-1)} \rangle}{\Delta T_E^{crit}} \right)^{\gamma_E}$ |
| | $f_D^{*(n)} = f_D^{*(n-1)} + A_D^{(n-1)} (1 - f_D^{*(n-1)}) f_D^{*(n-1)} \Delta t$ |
| | $f_E^{*(n)} = f_E^{*(n-1)} + A_E^{(n-1)} (1 - f_E^{*(n-1)}) f_E^{*(n-1)} \Delta t$ |
| | $f_D^{(n)} = (1 - \theta) f_D^{*(n)}$ |
| | $f_E^{(n)} = \theta f_E^{*(n)}$ |
| Update liquid & solid fractions: | |
| | $f_S^{(n)} = f_D^{(n)} + f_E^{(n)}$ |
| | $f_L^{(n)} = 1 - f_S^{(n)}$ |
| Update thermo-physical properties: | |
| | $C^{(n)} = C_L f_L^{(n)} + C_D f_D^{(n)} + C_E f_E^{(n)}$ |
| | $k^{(n)} = k_L f_L^{(n)} + k_D f_D^{(n)} + k_E f_E^{(n)}$ |
| Solve thermal problem: | |
| | $\sum_{e=1}^{ne} \int_{V_{(e)}} \mathbf{N}_{(e)}^T \left[C^{(n)} \left(\frac{T_{(e)}^{(n)} - T_{(e)}^{(n-1)}}{\Delta t} \right) + L \left(\frac{f_L^{(n)} - f_L^{(n-1)}}{\Delta t} \right) \right] dV_{(e)} +$ |
| | $\sum_{e=1}^{ne} \int_{V_{(e)}} k^{(n)} \mathbf{B}_{(e)}^T \nabla T_{(e)}^{(n)} dV_{(e)} = \sum_{e=1}^{ne} W_{(e)}^{ext}$ |
| Compute actual grain size: | |
| | $N_E^{(n)} = k_1 + k_2 \left(\dot{T}_E^{(n)} \right)^m$ |
| | $R_E^{(n)} = \sqrt[3]{\frac{3}{4\pi} \frac{f_E^{(n)}}{N_E^{(n)}}}$ |
| End loop | |

Table 2: Algorithm to solve the solidification analysis using the hypo-eutectic model

are characterized by different thermal modules and chemical compositions of the melt in order to study the response of the model to a wide range of process parameters and cooling rates. In particular, two different families of alloys have been studied: the eutectic ductile iron and the hypoeutectic grey cast iron. Hence, changing the chemical composition and the melt treatment, it is possible to reproduce different solidification behaviours, characterized by specific phase transformation temperatures and recalescence phenomena. To validate the model, the temperature field has been monitored during the solidification process by means of thermocouples located either in the melt or in the mold. The temperature evolution measured at the thermocouples has been compared to the numerical predictions.

The proposed model has been implemented into the software package COMET [22], a Finite Element (FE) based platform for the analysis of couple thermo-mechanical problems. Hence, the calculations have been performed in the enhanced version of this software developed at CIMNE (International Center for Numerical Methods in Engineering).

The proposed benchmarks have been characterized according to the process parameters and the material data as detailed in the corresponding references. Hence, it was not possible to assess the performance of the mixture rule model described in the above Sections due to the lack of data.

5.1 Quick Cup test

The Quick Cup test refers to the solidification of a small amount of cast iron poured into a little sand cup, commercially known as Quick Cup. This cup is characterized by a standard geometry which includes a *K-type* thermocouple inserted into a thin quartz tube and located at the hot spot of the specimen to measure the temperature evolution during the solidification process. The Quick Cup is one of the easiest and cheapest way to study the solidification of different casting alloys. It is extensively used in the foundry industry and it is the standard in DTA allowing for a quick quality control of the melt just before the pouring process [50]. The Quick Cup dimensions and the location of the thermocouple are shown in Figure 5.

In this work, two different melt compositions have been considered:

1. Quick Cup test-1: an *Eutectic* ductile iron with the following chemical composition: 3.52% *C*, 2.18% *Si*, 0.29% *Mn* and 0.01% *S*. The melt treatment consists of a *Mg* treatment (0.05%) and an inoculation.
2. Quick Cup test-2: a *Hypoeutectic* grey cast iron with the following chemical composition: 3.08% *C*, 2.14% *Si*, 0.82% *Mn*, 0.06% *S* and 0.05% *P* with an inoculation melt treatment.

The first test was chosen to assess the model for an eutectic solidification. The second test extends the assessment to a hypoeutectic alloy characterized by a dendritic austenite growth, where both undercooling and recalescence phenomena occur.

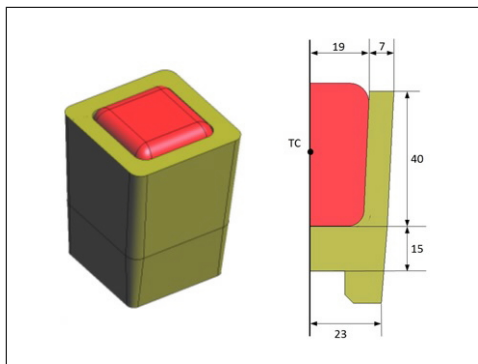


Figure 5: Quick-Cup test geometry: dimensions in [mm].

In this work, the geometry of the Quick Cup test has been simplified to an equivalent $2D$ geometry with the same thermal module as for the original $3D$ geometry. The objective of such simplification is the possibility to perform a fast $2D$ sensitivity analysis to calibrate both thermo-physical properties and the parameters of the solidification model.

The FE discretization is defined by 464 nodes and 833 triangular elements with an average mesh size of $2[mm]$. The time integration scheme uses a constant time-increment: $\Delta t = 1[s]$.

The simulation of the pouring phase has been omitted, so that only the solidification process has been considered. A uniform initial temperature of $1300^{\circ}C$ and $20^{\circ}C$ has been assumed for the casting and for the sand mold, respectively.

The Quick Cup is made of resin bonded sand. As in Celentano *et al.* [12], the following thermal properties of the mould have been adopted for the numerical simulations: density $1550 [kg/m^3]$, thermal conductivity $0.8 [W/mK]$ and specific heat $1000 [J/kgK]$. The thermal properties of both grey cast iron and ductile iron adopted in this work refer to those used in [12] and [10]: density $7000 [kg/m^3]$ and latent heat $228097 [J/kg]$. The specific heat and thermal conductivity are temperature-dependent material properties and they are reported in Table 3. Note that a higher thermal conductivity is assumed when the temperature is higher than the melting temperature, in order to take into account the natural convection in the liquid phase.

The temperature evolution during the solidification process obtained in the numerical simulation is driven by the Heat Transfer Coefficients (HTC) at boundaries of the ingot domain. On the one hand, the initial cooling of the melt after pouring is strictly related to the value HTC chosen at the casting/mould interface. On the other hand, the cooling phase after the solidification process is controlled by the HTC adopted for the heat dissipation by convection/radiation through the surrounding environment. Both values have been calibrated to match the experimental evidence. The resulting HTC used

| Temperature [$^{\circ}C$] | Specific Heat [J/kgK] | Temperature [$^{\circ}C$] | Conductivity [W/mK] |
|-----------------------------|---------------------------|-----------------------------|-------------------------|
| 20 | 500 | 420 | 41.0 |
| 600 | 750 | 560 | 37.0 |
| 800 | 750 | 700 | 33.6 |
| 1073 | 820 | 840 | 28.0 |
| 1155 | 840 | 980 | 22.5 |
| 1400 | 900 | 1120 | 18.8 |
| | | 1250 | 65.0 |

Table 3: Quick-Cup test: Thermal properties of cast iron

| Eutectic phase |
|-----------------------------------|
| $T_E^{start} = 1170^{\circ}C$ |
| $\Delta T_E^{crit} = 50^{\circ}C$ |
| $\beta_E = 1$ |
| $\gamma_E = 4$ |
| $\delta_E = 0$ |
| $f_E^0 = 0.1\%$ |

Table 4: Quick-Cup test: parameters used to characterize the eutectic model

for the heat exchange between casting and mold surfaces is $500 [W/m^2K]$. A convection/radiation HTC of $50 [W/m^2K]$ has been adopted to account for the heat dissipation through all the external surfaces of both the sand mould and the casting, exposed to the ambient temperature of $20^{\circ}C$.

The comparison between the experimental measurements and the prediction of the numerical model in term of the temperature evolution at the center of the casting is shown in Figures 6 and 7 for the eutectic and hypoeutectic alloy compositions, respectively.

In the case of eutectic ductile cast iron, 3 different phases can be clearly distinguished in the temperature evolution graph shown in Figure 6: (*i*) a fast cooling of the liquid, (*ii*) a plateau caused by the isothermal solidification of the eutectic phase and finally, (*iii*) a sudden change in the slope of the temperature curve, denoting the end of solidification and the beginning of the final cooling process.

The temperature curve resulting from the numerical analysis reproduces with great accuracy the three phases described above, including both the undercooling and the recalescence phenomena produced after the nucleation of the eutectic phase. The length of the solidification plateau (i.e. the solidification time) depends on the actual value of latent heat, which is specified as a material property, while the temperature evolution during the phase-change is strictly related to the solidification model adopted.

Table 4 shows the parameters used to feed the eutectic model proposed in this work.

It can be noted that T_E^{start} is a parameter of the model used to trigger

| Dendritic phase | Eutectic phase |
|----------------------------------|----------------------------------|
| $T_L^{start} = 1260^\circ C$ | $T_E^{start} = 1180^\circ C$ |
| $\Delta T_D^{crit} = 40^\circ C$ | $\Delta T_E^{crit} = 50^\circ C$ |
| $\beta_D = 1$ | $\beta_E = 1$ |
| $\gamma_D = 4$ | $\gamma_E = 4$ |
| $\delta_D = 0$ | $\delta_E = 0$ |
| $f_D^0 = 0.1\%$ | $f_E^0 = 0.1\%$ |
| $\theta = 0.4$ | |

Table 5: Quick-Cup test: parameters used to characterize the hypoeutectic grey cast-iron

the beginning of the eutectic transformation. This value corresponds to the change in the cooling rate of the liquid phase caused by the nucleation of the eutectic phase. The value of the eutectic temperature, T_E is lower than T_E^{start} and it corresponds to the temperature plateau during the solidification process: $T_E = 1150^\circ C$, characteristic for such alloy.

In the case of hypoeutectic grey cast iron, two different transformations take place during the solidification: firstly, the formation of the dendritic phase corresponding to the primary austenite γ' , followed by the nucleation and growth of eutectic cells composed by secondary austenite γ'' (also referred to as eutectic austenite) and graphite flakes [41]. Both transformations can be clearly observed in Figure 7, where the temperature measurement and the model prediction are compared. The dendritic growth of the primary austenite starts when the temperature drops below the liquidus temperature, referred to as T_L^{start} . A first plateau due to the latent heat release of this transformation can be observed around this temperature threshold. The model takes into account the increase of carbon content in the liquid due to the dendritic growth by reducing the actual value of the liquidus temperature according to the solid fraction evolution as stated in Eq. (36). This affects the cooling rate of the casting just before the eutectic transformation. Additionally, by modifying the parameter, θ , of the lever rule defined in Eq. (26), it is possible to split the latent heat delivery intended for the dendritic and the eutectic transformations. The value chosen for this parameter depends on the actual composition of the melt as well as on the inoculation treatment, allowing for an easy calibration of the model response.

The parameters adopted to characterize the hypoeutectic model are shown in Table 5.

A good agreement between the model prediction and the experimental evidence is achieved, capturing the temperature evolution and the cooling rate in the casting during the phase change, as well as the amount of latent heat released by the dendritic and eutectic transformation. Both dendritic and eutectic undercooling and recalescence phenomena are reproduced with remarkable accuracy.

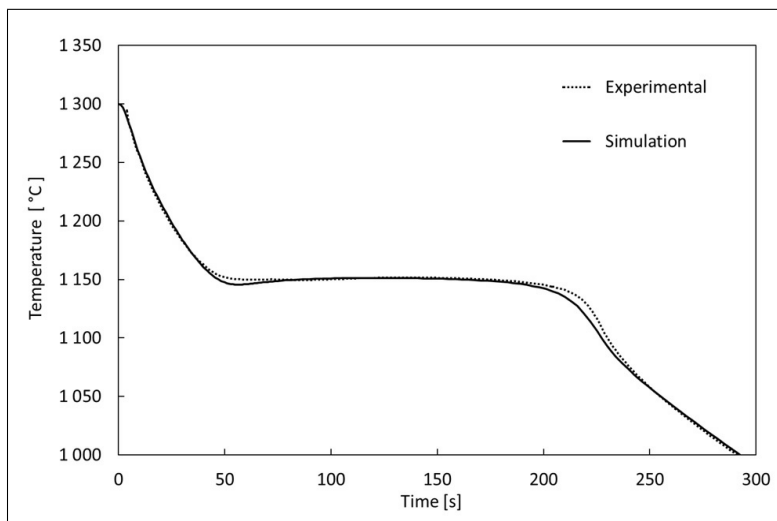


Figure 6: Quick-Cup test: Eutectic ductile cast iron. Temperature evolution at the hot-spot during the solidification process

5.2 Y-Shape test

The Y-Shape casting refers to a test presented by Celentano et al. [12], and is repurposed in this work to validate the solidification model for hypoeutectic grey cast iron.

The geometry and the dimensions of the casting are shown in Figure 8. Specimens of this shape are commonly used for the mechanical characterization of different alloys [7]. The top part of Y-Shape geometry works as a simple riser to avoid porosities in the lower part. Hence, it is possible to extract cylindrical samples from the bottom part free of casting defects and showing a good structural integrity. During the casting process, a thermocouple, denoted by *TCY*, is placed at the mid-section of the lower part of the casting sample in order to study the temperature evolution during the solidification. Note that this is not the hot spot of the casting. Because of this, the cooling conditions observed in the Y-Shape test are not the same as for the Quick-Cup test. Furthermore, this benchmark test has larger thermal module with longer solidification times, more representative of industrial foundry components.

The analysis is carried out in *2D* with a FE discretization consisting of 2004 triangular elements and 1058 nodes and a time-increment of: $\Delta t = 1[s]$. The average mesh sizes adopted are $4[mm]$ and $8[mm]$ for the casting and the mould, respectively.

The mold is made of resin bonded sand with material properties similar to the ones used for the Quick Cup test. The main differences lie in the different degree of sand compaction and humidity content. According to [12], the density is set to $1550 [kg/m^3]$, the specific heat is higher: $c = 1300 [J/kgK]$ and, finally,

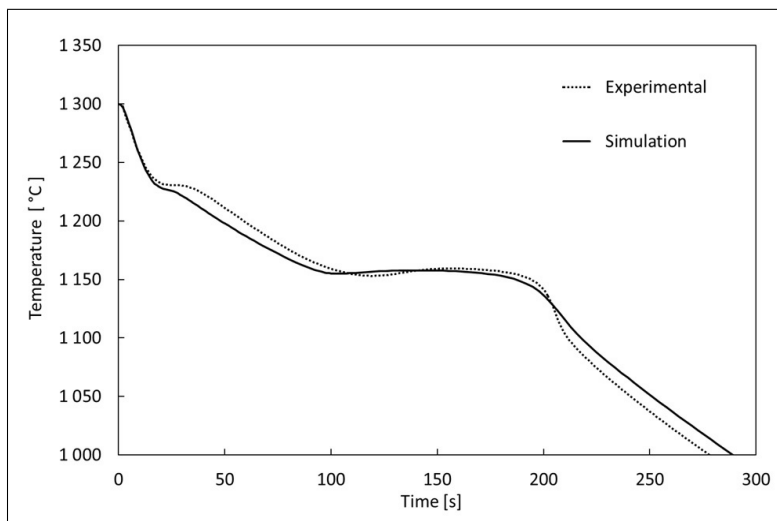


Figure 7: Quick-Cup test: Hypoeutectic grey cast iron. Temperature evolution at the hot-spot during the solidification process

the thermal conductivity is a temperature-dependent properties as shown in Table 6.

The casting alloy is a hypoeutectic grey cast-iron with a much higher carbon content compared to the Quick Cup test-2, so that a different solidification behaviour is expected. The reported chemical composition is the following: 3.45% *C*, 2.4% *Si*, 0.66% *Mn*, 0.014% *S* and 0.017% *P* with an inoculation melt treatment. Nevertheless, the same thermophysical material properties have been used as for the Quick-Cup test. The differences between the two casting alloys are reflected in the parameters adopted for the solidification model as shown in Table 7.

The pouring temperature is 1370°C , used as homogeneous initial temperature for the heat transfer analysis. The *HTC* coefficients used to characterize the heat flux between casting and mould as well as used for the heat convection model are the same as for the Quick Cup test.

Figure 9 shows a notable agreement between the experimental measurements and the corresponding numerical results in terms of temperature evolution at the thermocouple location TCY. Due to the higher carbon content of the Y-Shape test, the primary austenitic phase has a smaller impact on the solidification trend than in the Quick-Cup test, showing a lower temperature of liquidus and a much smaller temperature plateau corresponding to the dendritic transformation. This is reflected in the lower value of T_L^{start} as well as the lower value of the θ parameter adopted.

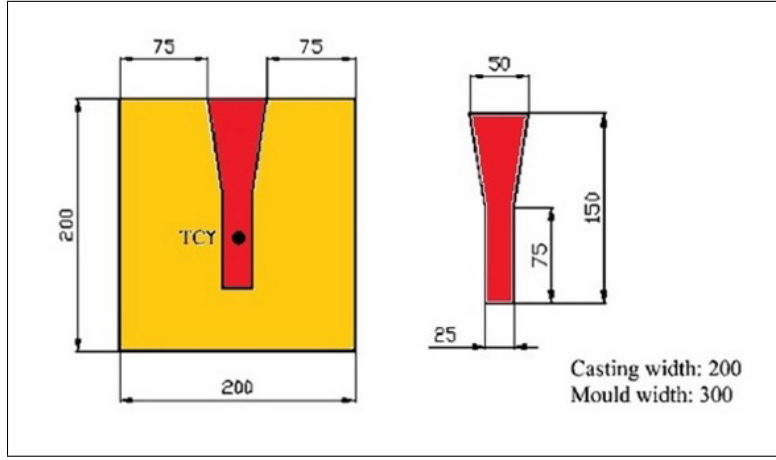


Figure 8: Y-Shape test geometry. Dimensions (in mm) of the casting equipment. TCY denotes the thermocouple location.

| Temperature [$^{\circ}C$] | Conductivity [W/mK] |
|-----------------------------|-------------------------|
| 20 | 0.54 |
| 300 | 0.57 |
| 500 | 0.65 |
| 700 | 0.79 |
| 900 | 1.00 |
| 1100 | 1.26 |
| 1300 | 1.59 |

Table 6: Y-Shape test: thermal conductivity of the resin bonded sand

5.3 Cubes Test

The Cubes test refers to the casting setting presented by Salsi et al. [43]. A cluster of 7 cubes of different sizes: 60, 75, 100, 120, 150, 180 and 210 [mm], respectively, is instrumented and an eutectic ductile iron alloy is used for the casting operation. The cubes are labeled with the numbers 1 to 7 according to their ascending size as shown in Figure 10. The mold dimensions are: 1200×1600 [mm²] and 640 [mm] height. The FE discretization consists of 1391 nodes and 2624 tetrahedral elements. The average mesh sizes are: 3, 5 and 10[mm] for the three cube sizes of 60, 100 and 180[mm], respectively. The time increment used is: $\Delta t = 1[s]$.

This casting experiment was designed to obtain a wide range of solidification conditions due to the increasing thermal modules and, consequently, lower and lower cooling rates according to the cubes size. Hence, a wide range of microstructures and mechanical properties were obtained. The temperature evolution during the solidification has been recorded at the hot spot (center) of

| Dendritic phase | Eutectic phase |
|----------------------------------|----------------------------------|
| $T_L^{start} = 1215^\circ C$ | $T_E^{start} = 1170^\circ C$ |
| $\Delta T_D^{crit} = 40^\circ C$ | $\Delta T_E^{crit} = 70^\circ C$ |
| $\beta_D = 1$ | $\beta_E = 1$ |
| $\gamma_D = 4$ | $\gamma_E = 4$ |
| $\delta_D = 0$ | $\delta_E = 0$ |
| $f_D^0 = 0.1\%$ | $f_E^0 = 0.1\%$ |
| $\theta = 0.25$ | |

Table 7: Y-Shape test: parameters used to characterize the hypoeutectic alloy

| Dendritic phase | Eutectic phase |
|----------------------------------|-----------------------------------|
| $T_L^{start} = 1173^\circ C$ | $T_E^{start} = 1172^\circ C$ |
| $\Delta T_D^{crit} = 30^\circ C$ | $\Delta T_E^{crit} = 100^\circ C$ |
| $\beta_D = 1$ | $\beta_E = 1$ |
| $\gamma_D = 4$ | $\gamma_E = 4$ |
| $\delta_D = 0$ | $\delta_E = 0$ |
| $f_D^0 = 0.1\%$ | $f_E^0 = 0.1\%$ |
| $\theta = 0.075$ | |

Table 8: Cubes test: Parameters used to characterize the solidification model

each cube by means of different thermocouples (*K-type* chrome/aluminum) with alumina shielding to protect them against prolonged expositions to high temperatures. The detailed description of the experimental setting, materials, methods and experimental measurements can be found in [43]. Additional information about the metallurgical and mechanical properties and the microstructure obtained for the different cubes of the casting are reported in [17].

This test allows for validating the solidification model in the case of this more complex casting processes as well as to check the model accuracy when dealing with very different thermal modules.

The casting alloy is a ductile iron with a carbon content close to the eutectic. The chemical composition is: 3.72% *C*, 2.19% *Si*, 0.19% *Mn*, 0.048% *Mg*, 0.001% *S* and 0.025% *P* with inoculation melt treatment and *Mg* addition. The thermophysical properties of the cast-iron are the same as for Quick-Cup test-1. If we compare the two alloys, the Cubes test presents a higher carbon and a lower silicon content. Table (8) shows the parameters used to characterize the solidification model.

The mold is made of green sand and the same thermal properties used in [43] have been adopted for the heat transfer analysis presented in this work: density: 1370 [kg/m^3], specific heat: 1030 [J/kgK]. The thermal conductivity is defined as a temperature-dependent property as shown in Table 9.

Despite of a pouring temperature of $1350^\circ C$, after the mould filling operation, the temperature field is not uniform. Hence, the initial temperature for the following solidification and cooling phases is different for each cube.

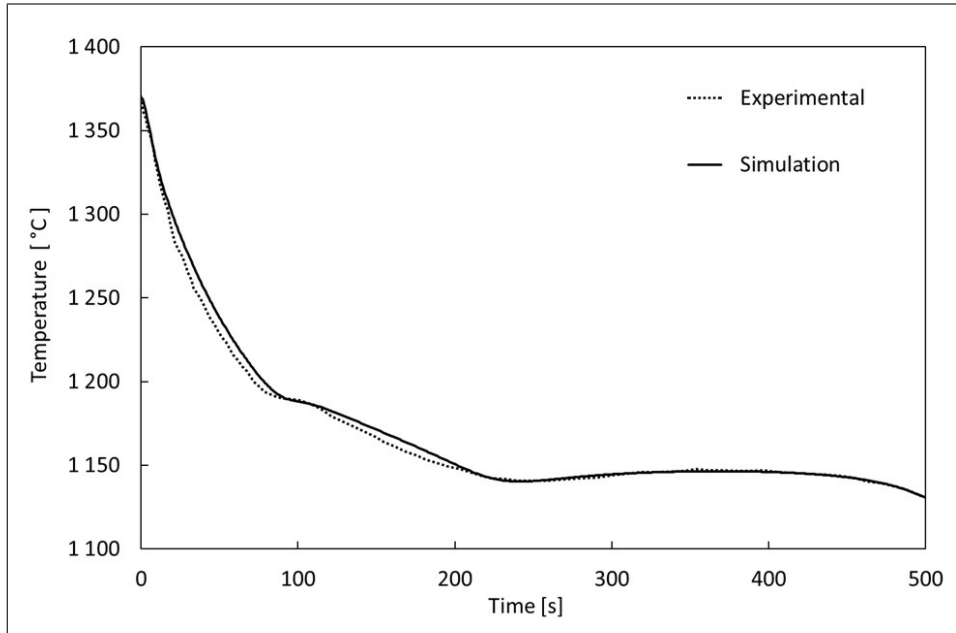


Figure 9: Y-Shape test. Temperature evolution at the thermocouple location TCY during the solidification process: Experimental measurement vs. Numerical result.

Figure 11 shows the temperature evolution recorded at the thermo-couples 1, 3 and 6 belonging to the cubes of 60, 100 and 180 [mm] and compares them with the numerical results. The measured temperatures show a first latent heat release previous to the eutectic solidification which is related to the formation of a small amount of primary austenite phase (γ'). Hence, the hypoeutectic model has been calibrated adopting a small value: $\theta = 0.075$ for the partition ratio. Once again, the solidification model proposed presents a good agreement with the experimental evidence in terms of cooling rates, solidification times, undercooling and recalescence phenomena for the 3 cubes, each one characterized by a different thermal module. More in detail, it is possible to observe how the undercooling and the recalescence are more pronounced for the smaller thermal modules. Contrarily, the temperature of the eutectic plateau increases according to the size (thermal module) of the cubes. All these phenomena are well captured by the proposed model.

5.3.1 Microstructural analysis

The objective of this casting experiment is the characterization of the ductile cast-iron for different cooling conditions and their influence on the final metallurgical properties in terms of nodule density and grain size distribution. Hence,

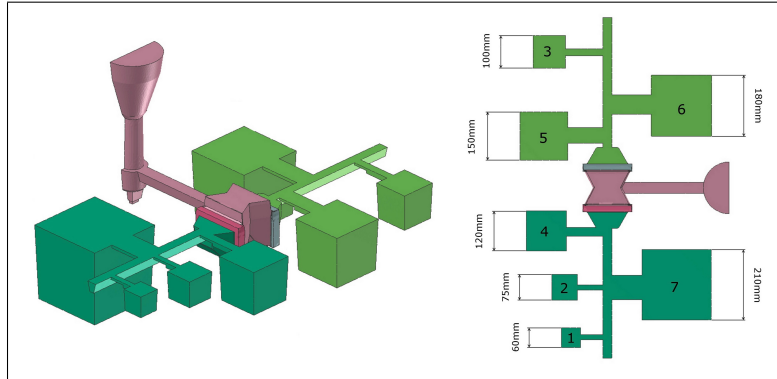


Figure 10: Cubes Test geometry. Dimensions (in mm) of the cubes in the casting experience.

| Temperature [$^{\circ}C$] | Conductivity [W/mK] |
|-----------------------------|-------------------------|
| 20 | 0.40 |
| 200 | 0.45 |
| 400 | 0.51 |
| 705 | 0.59 |
| 1005 | 0.77 |
| 1300 | 1.13 |

Table 9: Cubes test: thermal Conductivity of the Green Sand mold

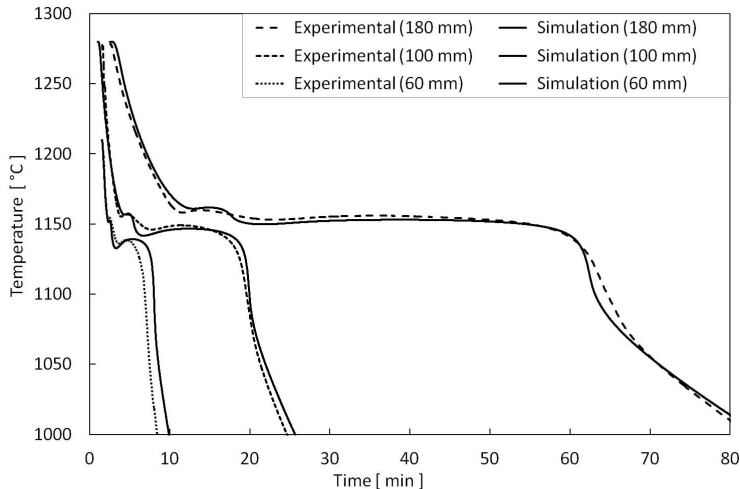


Figure 11: Cubes Test: Evolution of the temperature field during the solidification. Comparison between the experimental measurements and the numerical results for the cubes 1,3 and 6.

in the Cubes test the sensitivity to the different cooling conditions depends on: (i) the size of each cube; (ii) the distance from the center (thermal center) of the specimen. The outcome of this experimental campaign is detailed in [17].

The general trend in the experimental data shown in Figure 12 presents some fluctuation due to measurement uncertainties in the optical analysis. Moreover, the microstructure is affected by some undesired phenomena such as the local segregation, the presence of microporosity or the degeneration of the graphite nodules near the mold surfaces due to the sulphur content of the sand mould.

The experimental measurements show a higher density of graphite nodules for the smaller cubes or near the external surfaces according to the corresponding higher cooling rates. Similarly, the grain size decrease with the distance from the center of the cubes. It is important to note that the radius of the eutectic grain has been obtained multiplying the radius of the graphite nodule by a factor of 2.4 that is assuming a constant ratio between the size of the austenitic shell and graphite nodule for eutectic ductile irons [46].

These results have been used to calibrate the nucleation law in Eq. (19) and the corresponding nucleation parameters are reported in Table 10. The average grain size (within the hypothesis of graphite nodules surrounded by equiaxial austenitic shells) has been estimated using Eq. (20).

The comparison between the experimental data and the numerical predictions for cubes 1, 3 and 6 is shown in Figure 12. In this figure both the nodules density and the average grain size are presented as a function of the distance from the center of each of the 3 casting samples selected. There is a good

| Nucleation parameters |
|-----------------------|
| $K_1 = 236.5$ |
| $K_2 = 53.5$ |
| $m = 1$ |

Table 10: Cubes test: best suitable parameters for the nucleation law

agreement between the experiments and the numerical analysis even if the eutectic grain size predicted is slightly larger than the measurements. This can be attributed to the specific technique adopted for the $2D$ optical analysis. In fact, using this method, the average grain size refers to a generic section of the casting sample where the cutting plane divides the eutectic grains, leading to a systematic underestimation of their real sizes.

6 Conclusions

In this work, a novel solidification model suitable for both eutectic and hypoeutectic alloy compositions is described. The latent heat release is not defined by a generic temperature-dependent solid fraction function nor obtained from meso or microscale metallurgical models. Instead, a phenomenological model is introduced, depending on apropos evolution laws for both the dendritic and the eutectic phases. Hence, the latent heat released by the different phases evolving during the liquid-to-solid phase-change is controlled by ad-hoc Avrami-type functions defined for each phase.

The model allows to reproduce the recalescence phenomena observed during the solidification process as well as the thermal undercooling at the beginning of the phase-change.

The effects induced by the increase in the carbon content observed during the solidification process has also been considered modifying the actual liquidus temperature according to the solidification of the austenitic phase.

The model is complemented by defining a mixture rule accounting for the different thermophysical material properties of all the phases which coexist during the solidification process.

Finally, the average grain size (under the hypothesis of equiaxial grain growth) resulting from the microstructure evolution during the phase-change process is obtained a-posteriori by specifying a suitable nucleation law to estimate the actual nucleation density.

The proposed model is tested by reproducing the solidification patterns of both eutectic and hypoeutectic alloys. Firstly, the model has been calibrated considering simple castings as the Quick Cup test and the Y-shape test. Later, the numerical model is validated using the Cubes test, a casting experiment closer to the foundry production. The comparison between the numerical results and the experimental evidence shows a remarkable accuracy in terms of both temperature evolution and metallurgical features.

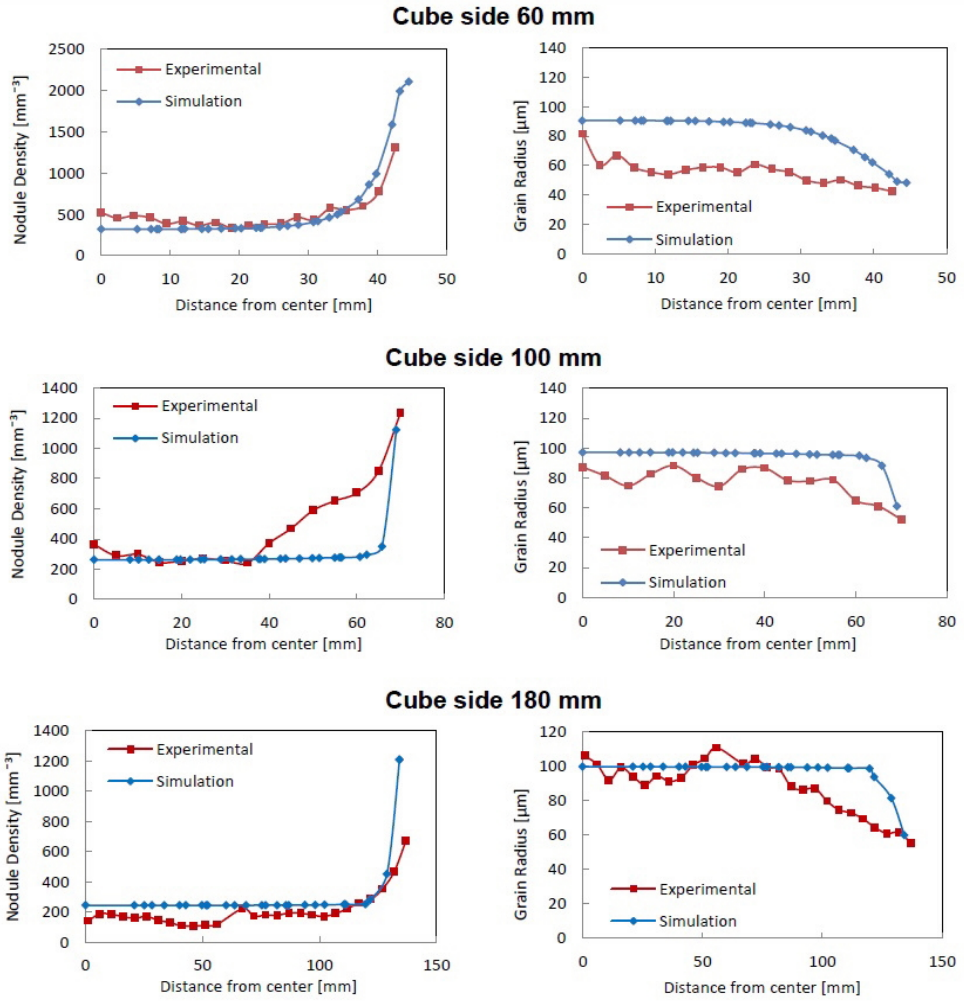


Figure 12: Cubes Test Microstructures. Experimental measurements and numerical result for microstructural main features (density of nodules and average grain radius) along a profile from the center to a vertex of cubes of 60,100,180 mm side

7 Acknowledgments

The financial support from the EU under the project: *Robust and Flexible Cast Iron Manufacturing (FLEXICAST)* within the 7th Framework Programme – Factories of the Future (Ref. NMP-2012-ICT-FoF) is gratefully acknowledged.

The collaboration with the Department of Industrial Engineering (DIN) of the University of Bologna as well as the foundry expertise from ProService-Tech is also gratefully acknowledged.

The Marie Skłodowska-Curie Grant No. 746250 received within the EU research and innovation programme is gratefully acknowledged.

References

- [1] Agelet de Saracibar C., Cervera M. and Chiumenti M., On the formulation of coupled thermoplastic problems with phase-change, *International journal of plasticity*, 15 (1999) 1-34.
- [2] Agelet de Saracibar C., Cervera M. and Chiumenti M., On the constitutive modeling of coupled thermomechanical phase-change problems, *International Journal of Plasticity*, 17 (2001) 1565-1622.
- [3] Agelet de Saracibar C., Chiumenti M. and Cervera M., Current developments on the coupled thermomechanical computational modeling of metal casting processes, *Int. J. on Comp. Methods in Material Science*, 6(1-2) (2006) 1-11.
- [4] Avrami M., Kinetics of Phase Change. I. General Theory, *Journal of Chemical Physics*, 7(12) (1939) 1103–1112.
- [5] Avrami M., Kinetics of Phase Change. II. Transformation-Time Relations for Random Distribution of Nuclei, *Journal of Chemical Physics*. 8 (2) (1940) 212–224.
- [6] Avrami, M , Kinetics of Phase Change. III. Granulation, Phase Change, and Microstructure". *Journal of Chemical Physics*, 9(2) (1941), 177–184.
- [7] ASM metals handbook. Casting, Vol. 15. 9th edn, ASM Materials Park, Ohio (1988).
- [8] Boeri R., The solidification of ductile cast iron, PhD thesis, University of British Columbia, Canada, (1989).
- [9] Bower T.F, Brody H.D., Flemings M.C., Measurements of Solute Redistribution in Dendritic Solidification, *Transaction of the Metallurgical Society of AIME*, 236 (1966) 624-633.
- [10] Carazo F., Dardati M., Celentano D., Godoy L., Thermo-Metallurgical Modeling of Nodular Cast Iron Cooling Process, *Metallurgical and Materials Transactions B*, 43B (2012) 1579-1594.

- [11] Celentano D.J., Cruchaga M., A thermally coupled flow formulation with microstructural evolution for hypoeutectic cast-iron solidification, *Metallurgical and Materials Transactions B*, 30 (1999) 731-744.
- [12] Celentano D.J., Cruchaga M. and Schulz B., Thermal microstructural analysis of grey cast iron solidification: simulation and experimental validation, *Int. Journal of Cast Metal Research*, 18(4) (2005), 237-247.
- [13] Celentano D.J., Dardati P.M., Godoy L.A., Boeri R.E., Computational simulation of microstructure evolution during solidification of ductile cast iron, *International Journal of Cast Metal Research* 21 (6) (2008) 416-426.
- [14] Celentano D.J., Dardati P.M., Carazo F.D., Godoy L.A., Thermomechanical-microstructural modelling of nodular cast iron solidification, *Materials Science Technology*, 29(2) (2013) 156-164.
- [15] Cervera, M., Oliver, J., Prato, T. Thermo-chemo-mechanical model for concrete. I: Hydration and aging. *Journal of Engineering Mechanics*, 125(9) (1999) 1018-1027.
- [16] Cervera M., Agelet de Saracibar C. and Chiumenti M., Thermo-mechanical analysis of industrial solidification processes, *Int. Journal for Num. Methods in Engineering*, 46 (1999) 1575-1591.
- [17] Ceschini L., Morri Al., Morri An., Salsi E., Squatrito R., Todaro I., Tomesani L., Microstructure and mechanical properties of heavy section ductile iron castings: experimental and numerical evaluation of effects of cooling rates, *Int. Journal of Cast Metals Research*, 28(6) (2015), 365-374.
- [18] Charbon C., Rappaz M., in *Physical Metallurgy of Cast Iron V*, Lesoult G., Lacaze J., eds., Scitec Publications, Uetikon-Zurich, Switzerland, (1997) 453-460.
- [19] Chen I.G., Stefanescu D.M., Computer-Aided Differential Thermal Analysis of Spheroidal and Compacted Graphite Cast Irons. *AFS Trans.* 92 (1984) 947-964.
- [20] Chiumenti M., Agelet de Saracibar C. and Cervera M., On the Numerical Modelling of the Thermo-Mechanical Contact for Metal Casting Analysis, *Journal of Heat Transfer*, 130, (2008), 1-10.
- [21] Clyne T.W., The use of heat flow modeling to explore solidification phenomena, *Metallurgical Transactions B*, 13(3) (1982) 471-478.
- [22] Cervera M., Agelet de Saracibar C. and Chiumenti M., COMET: Coupled Mechanical and Thermal analysis, (2002) Data Input Manual, Version 5.0, Technical report IT-308. Available from <http://www.cimne.com/comet>
- [23] Coussy O. *Mechanics of porous media*. Wiley, New York (1995).

- [24] Crowley A.B., Numerical solution of stefan problems, *International Journal of Heat and Mass Transfer*, 21(2) (1978) 215-219.
- [25] Cruchaga M., Celentano D., A Thermally Coupled Flow Formulation with microstructural Phase-Change effects, *Computational Mechanics*, S. Idelsohn, E. Oñate, eds. CIMNE, Barcelona, Spain 1998.
- [26] Dantzig J.A. and Rappaz M., *Solidification*. EPFL Press, Lausanne, 2nd edition (2016).
- [27] Dardati P.M., Godoy L.A., Cervetto G.A., Paguaga P., Micromechanics Simulation during the Solidification of SG Cast-Iron, *Revista internacional de métodos numéricos para cálculo y diseño en ingeniería*, 21(4) (2005) 327-344. ISSN 0213-1315
- [28] Dardati P.M., Godoy L.A., Celentano D.J., Microstructural Simulation of Solidification Process of Spheroidal-Graphite Cast Iron, *Journal of Applied Mechanics*, 73(6) (2006), 977-983.
- [29] Desbiolles J., Droux J., Rappaz J. and Rappaz M., Simulation of solidification of alloys by the finite element method, *Computer Physics Reports*, 6(1-6), (1987) 371-383.
- [30] Gandin C., Rappaz M., A coupled finite element-cellular automaton model for the prediction of dendritic grain structures in solidification processes, *Acta Metallurgica et Materialia*, 42(7) (1994) 2233-2246.
- [31] Gandin C., Rappaz M., A 3D Cellular Automaton algorithm for the prediction of dendritic grain growth, *Acta Materialia*, 45(5) (1997) 2187-2195
- [32] Lesoult G., Castro M., Lacaze J., Solidification of Spheroidal Graphite Cast Irons I. Physical Modelling, *Acta mater.*, 46 (1998) 983-995.
- [33] Lacaze J., Castro M., Lesoult G., Solidification of Spheroidal Graphite Cast Irons II. Numerical Simulation, *Acta mater.*, 46 (1998) 997-1110.
- [34] Lacaze J., Solidification of Spheroidal Graphite Cast Irons: III. Microsegregation Related Effects, *Acta mater.* 47 (1999) 3779-3792.
- [35] Mahin K.W., Hanson K., Morris J.W., Comparative analysis of the cellular and Johnson-Mehl microstructures through computer simulation, *Acta Metallurgica*, 28(4) (1980) 443-453.
- [36] Morgan K., Lewis R.W. and Zienkiewicz O.C., An improved algorithm for heat conduction problems with phase change. *International Journal for Numerical Methods in Engineering*, 12 (1978) 1191-1195.
- [37] Oldfield W., A Quantitative Approach to Casting Solidification: Freezing of Cast Iron, *ASM Trans.* 59 (1966) 945-959.

- [38] Oliveira M.J., Malheiros L.F., Ribeiro C.A., Evaluation of the heat of solidification of cast irons from continuous cooling curves, *Journal of Materials Processing Technology* 92-93 (1999) 25-30.
- [39] Perez E., Celentano D., Oñate E., Simulacion del proceso de solidificacion de la fundicion gris considerando un modelo microestructural. Proceedings of: 3^o Congreso de metodos Numericos en Ingenieria, Zaragoza, Spain, June 1996.
- [40] Rappaz M., Modelling of microstructure formation in solidification processes, *International Materials Reviews*, 34(3) (1989) 93-123.
- [41] Rivera G.L., Boeri R.E., Sikora J.A., Solidification of gray cast iron, *Scripta Materialia* 50 (2004) 331–335.
- [42] Rolph D. Bathe K., An efficient algorithm for analysis of nonlinear heat transfer with phase changes, *International Journal for Numerical Methods in Engineering* 18 (1982) 119–134.
- [43] Salsi E., Squatrito R., Todaro I., Tomesani L., Process modeling and microstructure prediction validation of sand ductile iron castings, *Advanced Sustainable Foundry*, 71st World Foundry Congress, Bilbao, Spain. 19-21 May, (2014), ISBN: 978-84-617-0087-5.
- [44] Scheil E., Comments on the layer crystal formation, *Z Metallkd*, 34 (1942) 70-72.
- [45] Shamsundar N., Sparrow E., Analysis of Multidimensional Conduction Phase Change Via the Enthalpy Model, *J. Heat Transfer*, 97(3), (1975) 333-340.
- [46] Stefanescu D.M., Kanetkar C., in *Computer Simulation of Microstructural evolution*, Srolovitz D.J. ed. , TMS, Warrendale, PA (1985) 171-188.
- [47] Stefanescu D.M., Upadhya G., Bandypadhyay D., Heat Transfer-Solidification Kinetics Modeling of Solidification of Castings, *Metall Trans* **21A** (1990) 997.
- [48] Stefanescu D.M., Methodologies for Modeling of Solidification Microstructure and Their Capabilities, *ISIJ International*, 35(6) 1996 637-650.
- [49] Stefanescu D.M., Microstructure evolution, in *Modeling for casting and solidification processing*, Kuang-O Yu ed., RMI Titanium Company, Niles, Ohio (2001) 123-187.
- [50] *Thermal Analysis of Cast Iron*, Heraeus Electro-Nite International N.V.
- [51] Thevoz P., Desbioles L., Rappaz M., Modeling of equiaxed microstructure formation in casting, *Metallurgical Transactions A*, 20(2) (1989) 311-322.

- [52] Wessen M., Svensson I.L., Modeling of ferrite growth in nodular cast iron, Metallurgical and materials transactions A, 27(8), (1996) 2209-2220
- [53] Wetterfall S., Friedrichsson H. and Hillert M., Solidification process of nodular cast iron, J. Iron Steel Inst. 110 (1972) 323-333.